Appl. Phys. A (2014) 116:1065–1073
DOI 10.1007/s00339-013-8183-4

Applied Physics A
Materials Science & Processing

Nickel aluminate oxides/hydroxides by pulsed laser ablation of $NiAl_2O_4$ powder in water

Ya-Ting Chan · Chao-Hsien Wu · Pouyan Shen · Shuei-Yuan Chen

Received: 1 November 2013 / Accepted: 29 November 2013 / Published online: 11 December 2013

Abstract Submicron-sized $NiAl_{2+x}O_4$ fragments and nanocondensates of Ni-doped γ-Al_2O_3, Al-doped NiO and β-$Ni(OH)_2$ were synthesized simultaneously by pulsed laser ablation of $NiAl_2O_4$ powder in water and characterized using X-ray/electron diffraction and optical spectroscopy. The $NiAl_{2+x}O_4$ is Al-enriched spinel with dislocations and subgrains. The Ni-doped γ-Al_2O_3 spinel has paracrystalline distribution (i.e., with fair constant longitudinal spacing, but variable relative lateral translations) of defect clusters and intimate intergrowth of θ-Al_2O_3 and 2x($\bar{1}3\bar{1}$) commensurate superstructure. The Al-doped NiO has perfect cubo-octahedron shape and as small as 5 nm in size. The β-$Ni(OH)_2$ and 1-D turbostratic hydroxide lamellae occurred as a matrix of these oxide nanoparticles. The colloidal suspension containing the composite phases has a minimum band gap of 5.3 eV for potential photocatalytic applications.

1 Introduction

$NiAl_2O_4$, having a normal spinel-type structure with Al^{3+} in octahedral sites and Ni^{2+} in tetrahedral sites or partially inversed with Al^{3+} in both octahedral and tetrahedral sites [1], was commonly used as high-temperature fuel cell [2] and sensor materials such as catalyst support, which can provide a stabilizing effect while maintaining a high degree of chemical inertia [3, 4]. Nickel was particularly found to have much greater stability when supported on $NiAl_2O_4$ than on other supports [3]. In general, smaller particle size has beneficial higher (typically up to 100 m^2/g) specific surface area for catalytic applications of the $NiAl_2O_4$ support. Synthesis of nanosized $NiAl_2O_4$ particles is, thus, of great interest to such applications. The end members of $NiAl_2O_4$, i.e., NiO [5] and Al_2O_3 [6], were also used as catalytic supports.

The $NiAl_2O_4$ particles prepared by reactive sintering the powdery end members, i.e., NiO and α-Al_2O_3, at high temperature (1,100 °C) in air generally fall in submicron to micron size [7, 8]. As for the chemical synthesis of submicron to nanosized $NiAl_2O_4$ particles, it has been accomplished by the co-precipitation method [4], sol–gel process [9, 10], microwave treatment [11], ultrasonic treatment of precursor aqueous solution followed by high-temperature (950 °C) aging [12]. The expensive precursor phase and pollutant solution are the main shortages of these chemical methods. It is, thus, worthwhile to try an alternative clean synthesis of nanoparticles by pulsed laser ablation (PLA) in liquid.

Recently, PLA of ceramic powders in water was used for the clean synthesis of SnO_2 [13] and $CaCO_3$ [14] nanoparticles with dense structure and narrowed band gap. Here, this method is adopted to study the phase behavior of $NiAl_2O_4$ powders when subjected to PLA in water. We focused on: (1) the extent of $NiAl_2O_4$ powders fragmentation as nanosized particles without phase change, (2) the decomposition of $NiAl_2O_4$ powders as end-member nanoparticles with internal compressive stress, (3) the formation of a lamellar phase, which is related to the so-called layered double hydroxides (LDH) or anionic clays [15–18] as a precursor phase of spinel oxides [19, 20], and (4) the accompanied band gap change of the colloidal suspension.

Y.-T. Chan · C.-H. Wu · P. Shen
Department of Materials and Optoelectronic Science, National Sun Yat-sen University, Kaohsiung 80424, Taiwan, ROC

S.-Y. Chen (✉)
Department of Mechanical and Automation Engineering, I-Shou University, Kaohsiung 84001, Taiwan, ROC
e-mail: steven@isu.edu.tw

2 Experimental

NiO (99.995 %) and Al_2O_3 (99.9 %) powders in 1:1 molar ratio were thoroughly mixed in a beaker filled with de-ionized water and heated at 100 °C by a hot plate coupled with magnet stirring. The uniform powder mixtures were fired at 1,600 °C for 10 h to form $NiAl_2O_4$ powders in an open-air furnace followed by furnace cooling and then grinding using agate mortal and pestle to go through a sieve of 200 mesh.

A fixed amount (0.01 g) of the sieved $NiAl_2O_4$ powders in a silica test tube (0.8 cm in inner diameter and 10 cm in length) was combined with de-ionized water of 10-mm height for a total concentration of 3.2 mg/cc and then subjected to energetic Nd-YAG-laser (Lotis, 1,064 nm, beam mode: TEM00) pulse irradiation. In such experiments, the laser beam was focused to a spot size of 0.03 mm^2 on the specified water height at water level under laser pulse energy of 400 mJ/pulse using second harmonic excitation, i.e., 532 nm for better laser penetration in water. The Q-switch mode for specified pulse duration of 16 ns was adopted to achieve a peak power density of 8.35×10^{10} W/cm^2 (average power density 1.33×10^4 W/cm^2) at 10 Hz. Water refill and suspension shaking after every 5 min of PLA procedure were employed to ensure a uniform colloidal suspension upon energetic irradiation for an accumulated time of 30 min. The bluish colloidal suspension became dark blue and warmed up to ca. 50 °C after the PLA process (Appendix 1).

The sample of particles centrifuged from the colloidal suspension for a much larger quantity was then deposited on glass for identification by X-ray diffraction (XRD, SIEMENS D5000, Cu Kα at 40 kV, 30 mA and 3 s for each 0.05° increment from 20° up to 80° of 2θ angle). The crystal structures of the individual condensates collected on Cu grids overlaid with a carbon-coated collodion film were characterized by transmission electron microscopy (TEM, JEOL 3010 at 200 kV) based on bight field image (BFI), selected area electron diffraction (SAED) and lattice imaging coupled with point-count energy-dispersive X-ray (EDX) analysis.

The UV–Visible absorption of the colloidal suspension as-formed by PLA was characterized by the instrument of U-3900H, Hitachi with a resolution of 0.1 nm in the range of 190–900 nm. Raman spectra of the centrifuged condensates were made using He–Ne laser excitation (633 nm) having a spatial resolution of 1 μm (HORIBA HR800) to identify the structure units of the condensates in the range of 200–2,000 cm^{-1}. The centrifuged condensates were also mixed with KBr for Fourier transform infrared spectroscopy (FTIR, Bruker 66v/S, 64 scans in the range of 400–4,000 cm^{-1} with 4 cm^{-1} resolution) study of OH^- signature and phase change of the $NiAl_2O_4$ powder subjected to PLA in water.

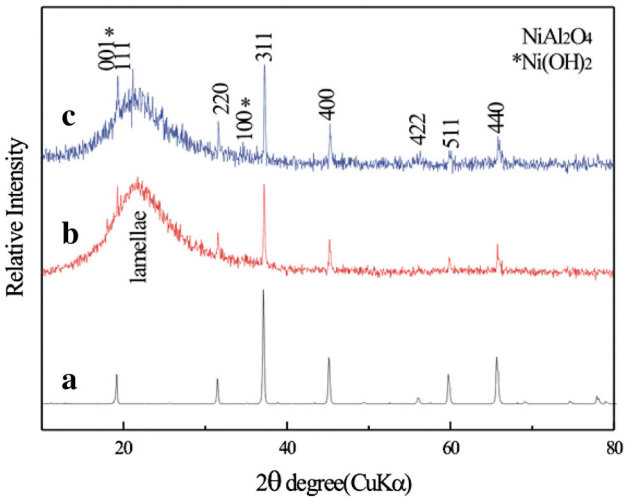

Fig. 1 XRD traces of *a* starting $NiAl_2O_4$ powder and that subjected to PLA at 10-mm water/focus height for *b* 5 min and *c* 20 min to form nanosized $NiAl_2O_4$, β-$Ni(OH)_2$ and a turbostratic lamellar phase (cf. text)

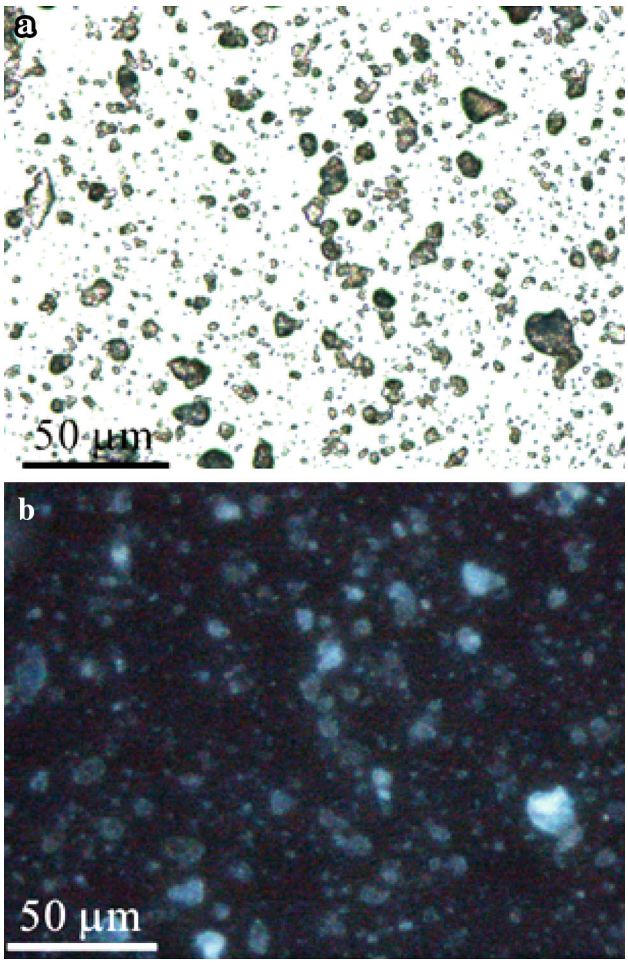

Fig. 2 Optical polarized micrograph of the sample produced by PLA of $NiAl_2O_4$ powder at 10-mm water/focus height for 20 min, under **a** open polarizer and **b** crossed polarizers

3 Results

3.1 XRD

XRD of the starting $NiAl_2O_4$ powders showed sharp diffraction peaks of the spinel structure (Fig. 1a), the same as that reported in JCPDS file #10-0339. The spinel diffraction peaks were considerably broadened and shift to higher 2θ for the powders subjected to PLA at 10 mm water/focus height for 5 min (Fig. 1b) and 20 min (Fig. 1c). Additional phases, i.e., β-$Ni(OH)_2$ (space group $P\ \bar{3}m1$) and a turbostratic lamellar phase with a rather broad diffraction at low 2θ angle (22° different from that peaked at 21° for the silica glass substrate), also showed up after such PLA treatments in water (Fig. 1b, c).

3.2 Optical and electron microscopy

Optical polarized microscopic observation of the $NiAl_2O_4$ powders subjected to PLA at 10 mm water/focus height for 20 min showed representatively that the powders became submicrons to ca. 20 microns in size and were equiaxed with facets (Fig. 2a). The relatively large-sized $NiAl_2O_4$ spinel particles showed slight optical anisotropy (Fig. 2b), i.e., with weak interference color under crossed polarizers according to Nesse [21], presumably due to grinding and/or PLA-induced strain.

The identity of the individual spinel particles was verified by TEM BFI (Fig. 3a) and SAED (Fig. 3b) of a representative submicron-sized $NiAl_{2+X}O_4$ particle produced by PLA of $NiAl_2O_4$ powder at 10 mm water/focus height for 20 min, showing well-developed $(1\bar{1}1)$ and (001) faces edge on in the [110] zone axis. This fragmented spinel particle also showed subgrain boundaries in DFI (Fig. 3c) and Al enrichment in comparison with the stoichiometric $NiAl_2O_4$ in EDX spectrum (Fig. 3d).

As for nanosized $NiAl_{2+X}O_4$ or Ni-doped γ-Al_2O_3 with spinel isostructure in the same TEM specimen, they were typically assembled in random orientation as a corrugated spherical particle (Fig. 4a) to give characteristic diffraction rings in SAED pattern (Fig. 4b). Point-count EDX analysis on this polycrystalline particle showed an overall

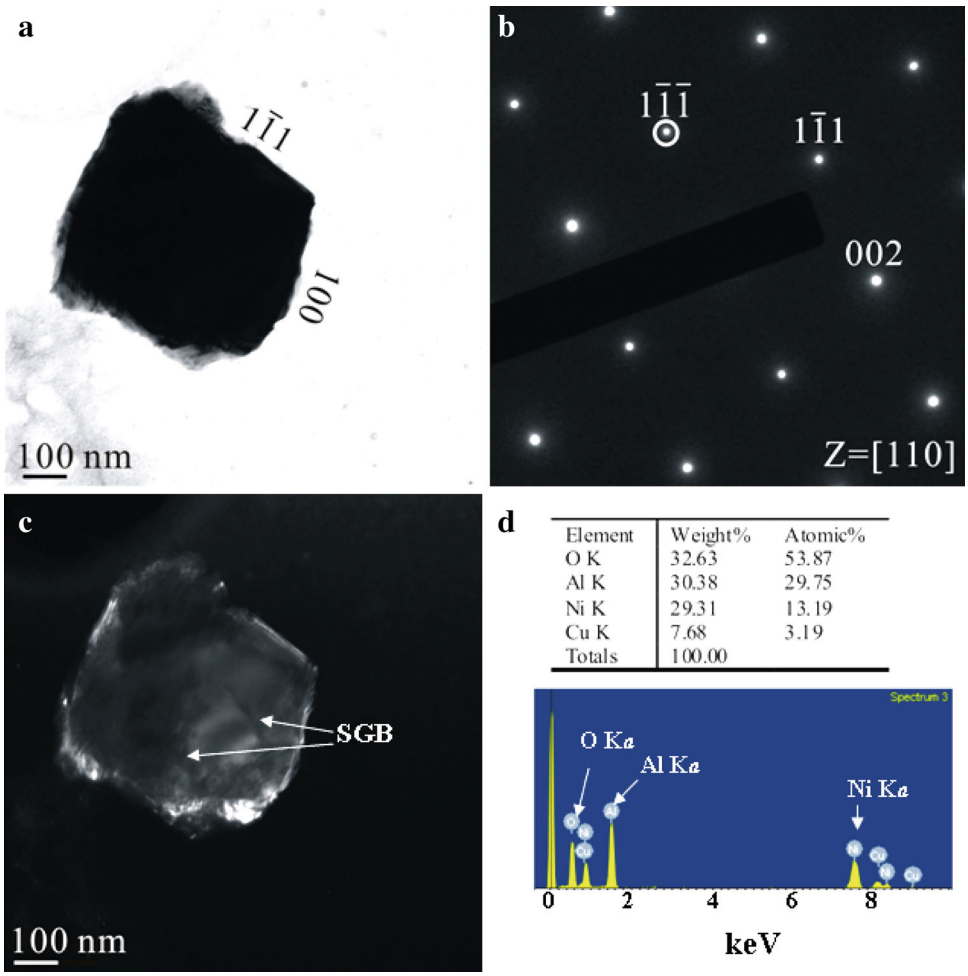

Fig. 3 TEM of a typical submicron-sized $NiAl_{2+X}O_4$ particle produced by PLA of $NiAl_2O_4$ powder at 10-mm water/focus height for 20 min: **a** BFI and **b** SAED pattern showing well-developed $(1\bar{1}1)$ and (001) faces edge on in the [110] zone axis, (**c**) DFI ($g = 1\bar{1}\bar{1}$ as circled) showing subgrain boundaries (SGB), (**d**) EDX spectrum showing Al enrichment than $NiAl_2O_4$ stoichiometry

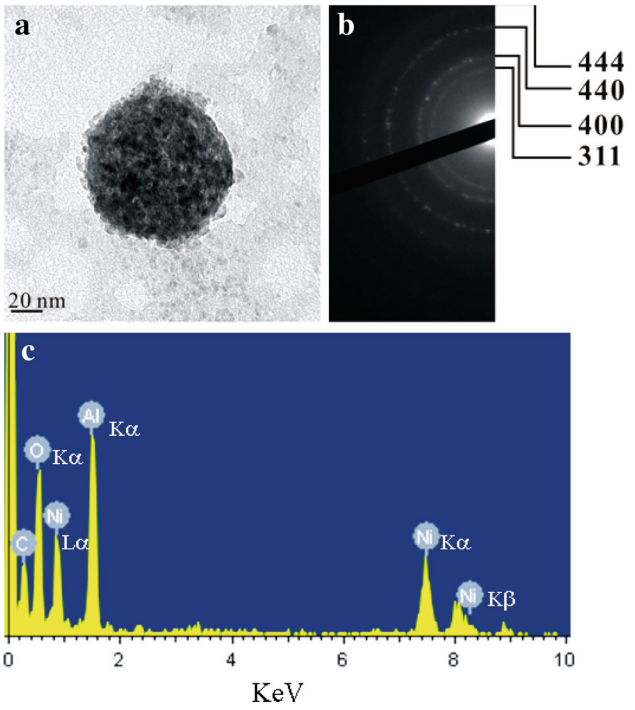

Fig. 4 TEM of a typical corrugated spherical particle consisting of nanosized $NiAl_{2+X}O_4$ and Ni-doped γ-Al_2O_3 with spinel isostructure, as produced by PLA of $NiAl_2O_4$ powder at 10-mm water/focus height for 20 min, **a** BFI, **b** SAED pattern and (**c**) EDX spectrum indicating an overall composition of Ni:Al:O = 1:3.7:7.6 atomic ratio in the formula $\sim M_2O_3$ having M/O = 0.62 and with M ca. 20 % Ni and 80 % Al, i.e., 20 % Al^{3+} being replaced by Ni^{2+} (cf. text)

composition of Ni:Al:O = 1:3.7:7.6 in atomic ratio, which can be represented by the formula $\sim M_2O_3$ having M/O = 0.62, where M is ca. 20 % Ni and 80 % Al, i.e., 20 % Ni^{2+} in substitution for Al^{3+}. Lattice image (Fig. 5a) coupled with 2D forward/inverse Fourier transform (Fig. 5b, c) of such spherical polycrystals showed that the individual $NiAl_{2+X}O_4$ or Ni-doped γ-Al_2O_3 phase has paracrystalline distribution of defect clusters with ca. 1 nm interspacing in the [011] zone axis of the spinel isostructure.

Lattice image (Fig. 6a) further indicated that the Ni-doped γ-Al_2O_3 also occurred as individual spherical nanoparticle, which tended to be encapsulated with a turbostratic lamellar shell. The 2D forward/inverse Fourier transform from the Ni-doped γ-Al_2O_3 core (Fig. 6b, c) showed intimate intergrowth of θ-Al_2O_3 (JCPDS file 11-0517) and 2x($\bar{1}3\bar{1}$) commensurate superstructure as well as misfit dislocations with (220) and ($3\bar{1}1$) half planes (Fig. 6). TEM lattice image (Fig. 7a) coupled with 2D forward/inverse Fourier transform (Fig. 7b, c) further identified an isolated NiO nanoparticle, which is as small as 5 nm in size with well-developed (010) and ($\bar{1}11$) faces sitting in a matrix of the 1D turbostratic lamellar phase more or less assembled to show Bragg diffraction.

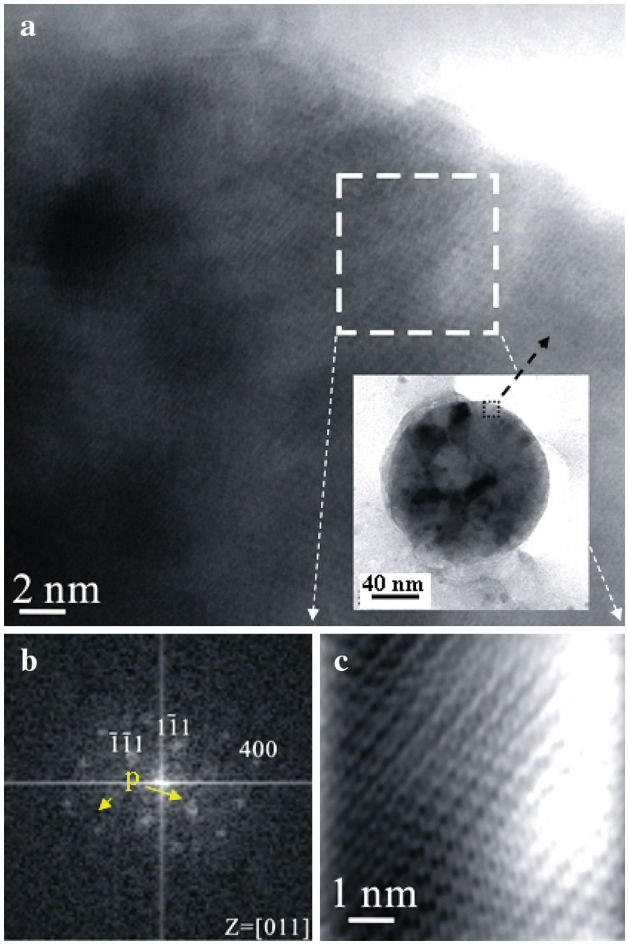

Fig. 5 TEM **a** lattice image enlarged from a spherical polycrystalline nanoparticle (*inset*) and **b**, **c** 2D forward/inverse Fourier transform of the square region, which contains Ni-doped γ-Al_2O_3 with the spinel-type structure having paracrystalline (denoted as P for side-band diffractions) distribution of defect clusters ca. 1 nm interspacing as viewed in the [011] zone axis in **c**. The same PLA specimen as in Fig. 4

3.3 Vibrational spectroscopy

The Raman spectra of the samples subjected to PLA at 10-mm water/focus height for 5 up to 20 min (Fig. 8) showed that the $NiAl_{2+X}O_4$ and Ni-doped γ-Al_2O_3 rich condensates/particles have E_g, T_{2g} and A_{1g} modes considerably different from that reported for the $NiAl_2O_4$ single or polycrystals [22] as compiled in Table 1. This indicates a considerable structure unit change of $NiAl_2O_4$ powders in accompaniment with their size miniature, densification, phase change and enhanced protonation/hydroxylation by the PLA process in water as addressed later.

The FTIR spectra of the $NiAl_2O_4$ powders subjected to PLA at 10 mm water/focus height for 5 and 20 min (Fig. 9a, b) showed a rather broad band at 719 cm^{-1}, which is due to tetrahedrally coordinated Al–O stretching in view of the assignment of Jeevanandam et al. [12] for

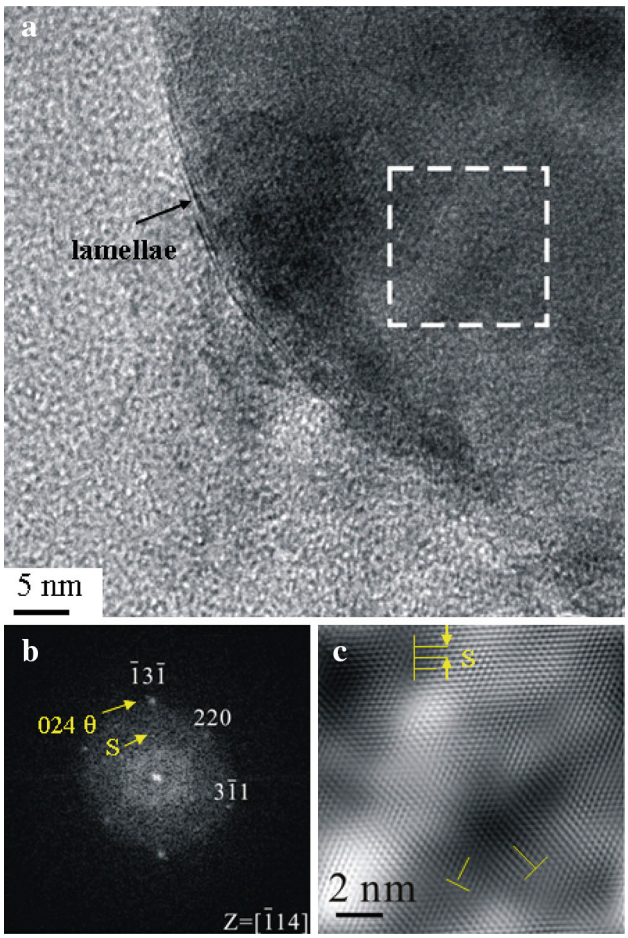

Fig. 6 TEM **a** lattice image and **b**, **c** 2D forward/inverse Fourier transform of the square region of a spherical Ni-doped and lamellae-encapsulated γ-Al_2O_3 particle with intimate intergrowth of θ-Al_2O_3 and 2x($\bar{1}3\bar{1}$) commensurate superstructure (denoted as S) as well as dislocations with (220) and ($3\bar{1}1$) half planes. The same PLA specimen as in Fig. 4

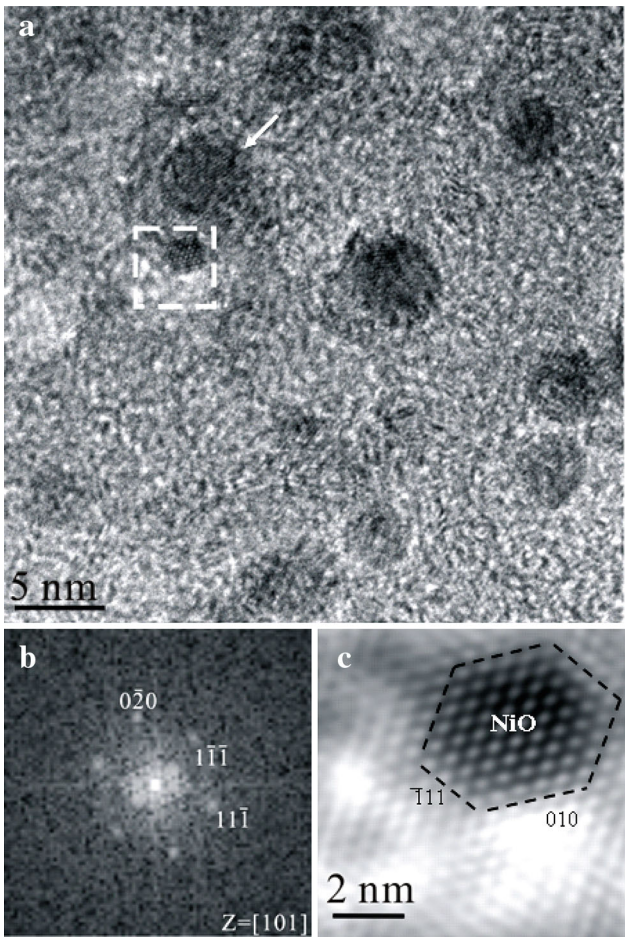

Fig. 7 TEM **a** lattice image and **b**, **c** 2D forward/inverse Fourier transform of the square region showing a 5-nm-sized NiO particle with well-developed (010) and ($\bar{1}11$) faces edge on in the [101] zone axis. Note 1D turbostratic lamellar phase in the matrix which showed significant Bragg diffraction contrast when well assembled (*arrow*). The same PLA specimen as in Fig. 4

nickel aluminate spinel prepared by a sonochemical method. The additional bands at 3,415 and 1,629 cm^{-1} can be attributed to OH^- species and absorbed water, respectively; whereas 1,382 cm^{-1} C–H asymmetric stretching of CH_3 in the relic cleaning agent EtOH. In comparison with the nickel aluminate spinel prepared by sonochemical synthesis [12], there is a considerable shift of IR bands for the present sample (Table 2) apparently due to significant phase and size changes of $NiAl_2O_4$ powders by the PLA process in water.

3.4 UV–Visible absorption

The representative colloidal suspension prepared by PLA of $NiAl_2O_4$ powder at 10-mm water/focus height for 20 min showed a significant absorption in UV range, which corresponds to a minimum band gap of 5.32 eV based on its intersection with the base line at 232.9 nm (Fig. 10). By comparison, the minimum band gap is 5.82 eV for the starting colloidal sample based on its UV–Visible absorbance trace (not shown) [23].

4 Discussion

4.1 Phase selection during PLA of $NiAl_2O_4$ powder in water

The present experimental results indicated that $NiAl_2O_4$ powders subjected to PLA in water were either fragmented as micron-sized spinel particles with slight optical anisotropy or decomposed as atom clusters for further condensation and nucleation as hydroxides, i.e., 1D lamellar phase and β-$Ni(OH)_2$, and close packed oxides, i.e., Al-doped NiO and Ni-doped γ-Al_2O_3.

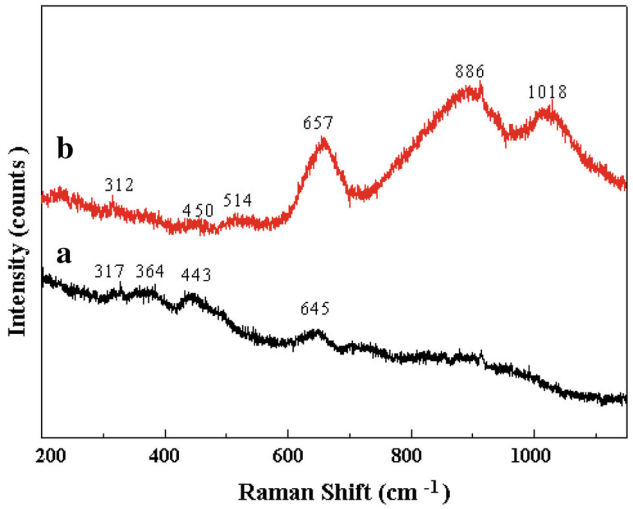

Fig. 8 Raman spectra of the sample produced by PLA of $NiAl_2O_4$ powder at 10-mm water/focus height for *a* 5 min and *b* 20 min, presumably probed on local areas with enriched $NiAl_{2+x}O_4$ and Ni-doped γ-Al_2O_3 ,respectively

Table 1 Raman bands of spinel isostructures in NiO–Al_2O_3 binary system

$NiAl_{2+x}O_4$[a] (cm^{-1})	Ni-doped γ-Al_2O_3[b] (cm^{-1})	$NiAl_2O_4$[c] (cm^{-1})	Mode
317, 364	312	326, 70	E_g
443	450	468	T_{2g}
NA	514	564	T_{2g}
645	657	686	A_{1g}
NA	886	800–830	A_{1g}
NA	1,018	866	A_{1g}

[a] and [b] samples produced by PLA of $NiAl_2O_4$ powders at 10-mm water/focus height for 5 and 20 min, respectively, of this work; [c] single and polycrystalline $NiAl_2O_4$ after Laguna-Bercero et al. [22]

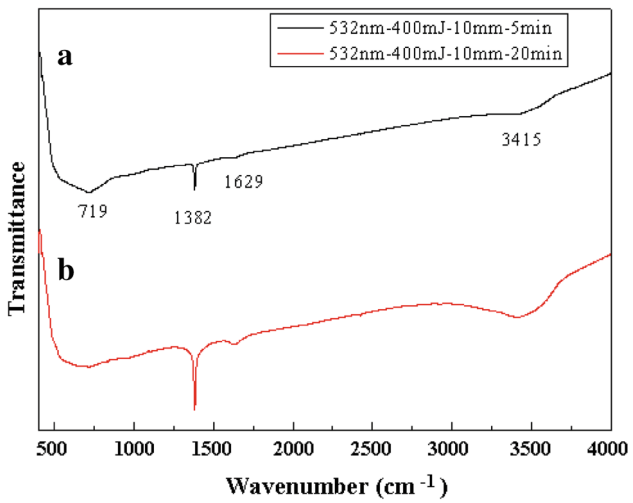

Fig. 9 FTIR spectra of the sample produced by PLA of $NiAl_2O_4$ powder at 10-mm water/focus height for *a* 5 min and *b* 20 min

Table 2 Infrared bands of $NiAl_2O_4$ powders subjected to PLA at 10-mm water/focus height for 5 to 20 min

PLA sample, this work (cm^{-1})	Jeevanandam et al. [12][a] (cm^{-1})	Mode
719	722	Tetrahedrally coordinated Al–O stretching
1,382	1,390	C–H asymmetric stretching of CH_3 and/or ν_3 of CO_3^{2-}
1,629	1,640	Bending vibration of interlayer water
3,415	3,450	Stretching of OH group

[a] nanosized particles of nickel aluminate spinel by a sonochemical method [12]

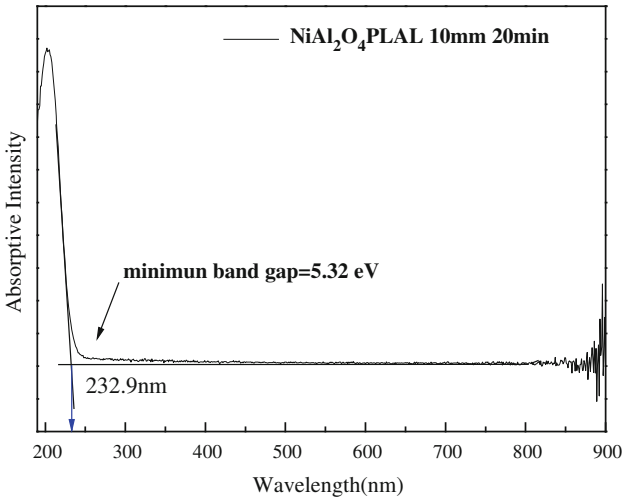

Fig. 10 UV–Visible absorption spectrum of the colloidal suspension produced by PLA of $NiAl_2O_4$ powder at 10-mm water/focus height for 20 min

The 1D lamella could improve its crystallinity to form β-$Ni(OH)_2$, which belongs to LDH or anionic clays [15–18] known as a precursor phase of spinel oxides [19, 20]. The condensed LDH is Ni-based as β-$Ni(OH)_2$ rather than Al-based in the present PLA of $NiAl_2O_4$ power in de-ionized water. This indicates that Ni-based LDH are the energetically favored hydroxides at nanoscale in the present aqueous conditions of the PLA process. Such conditions are: (1) Eh = 0 and pH = 7 in de-ionized water without an applied voltage, (2) temperatures around ~1,000 °C under radiant heating of the PLA process, which accounts for the coalescence of oxide nanocondensates such as originally suggested for TiO_2 [24], and (3) shock pressure up to several GPa in view of the formation of dense oxides, such as α-PbO_2 type SnO_2 by PLA in water [13].

As for the phase selection of close packed oxides in nanosize, Ni-doped γ-Al_2O_3 with spinel-type structure is

energetically more favorable than Al-doped NiO with rock salt-type structure. In this regard, thermodynamic considerations indicated that transition metal oxides have a lower surface energy for spinel structure (e.g., 1.44 J/m^2 for Fe_3O_4, 1.96 J/m^2 for Co_3O_4, 1.8 J/m^2 for $MgAl_2O_4$ and 1.53 J/m^2 for γ-Al_2O_3 with spinel isostructure) than rock salt-type structure (e.g., 3.5 J/m^2 for NiO, 3.57 J/m^2 for CoO, and 3.6 J/m^2 for $Fe_{0.947}O$) [25]. It is, thus, reasonable for Al-doped NiO nuclei to change into Ni-doped γ-Al_2O_3 and/or $NiAl_{2+X}O_4$ when the condensates were coarsened or coalesced for interdiffusion and hence composition modification. The Ni-doped γ-Al_2O_3 was allowed to form paracrystalline distribution of defect clusters and intimate intergrowth of θ-Al_2O_3 and commensurate superstructure when coarsened and stressed. Whereas α-Al_2O_3, with corundum-type structure and a relatively high surface energy of 2.6 J/m^2 [26], is not favorable unless further coarsened to have specific surface areas <75 m^2/g at temperatures such as 527 °C [26] or via kinetic phase change in a dynamic process [27]. In any case, the nanocondensates tended to assemble as spherical polycrystals upon radiant heating of the PLA process so that the total surface area can be minimized.

4.2 Composition and defects due to particle fragmentation and condensate doping by the PLA process

The combined optical polarized microscopy and TEM observations indicated that submicron- to micron-sized nickel aluminate spinel particles and Ni-doped γ-Al_2O_3 with spinel isostructure have lattice imperfections by the PLA process in water. The dislocations and subgrains of relatively large-sized $NiAl_{2+X}O_4$ fragments with significant Al enrichment than stoichiometric $NiAl_2O_4$ (Fig. 3) can be attributed to shock and radiant heating effects upon laser pulses in water. In fact, the fragmented $NiAl_{2+X}O_4$ spinel particle was determined by point-count EDX analysis to have ca. 70 mol % of Al_2O_3 component, i.e., Ni:Al:O = 1:2.26:4.08 atomic ratio in the formula $\sim NiAl_{2.3}O_4$. This solubility level is close to that allowed for $NiAl_{2+X}O_4$ at ca. 2,000 °C according to the NiO–Al_2O_3 binary phase diagram (Appendix 2) [28]. However, the temperature due to radiant heating of a typical PLA process in air or water was believed to be around 1,000 °C to assemble/coalesce the oxide nanocondensates as a close packed manner analogous to the case of TiO_2 [24]. Such a discrepancy can be reconciled by the shock-induced solute trapping effect to enhance solid solubility as the case of TiO_2 nanocondensates with enhanced dissolution of NiO [29] and Cr_2O_3 [30] by the PLA process in air.

The Ni-doped γ-Al_2O_3 nanocondensates have paracrystalline distribution of defect clusters in spinel structure (Fig. 5) analogous to that occur in $Co_{3-\delta}O_4$ spinel with or without Zr^{4+} dopant by a sintering route [31, 32] and γ-$Al_{2-\delta}O_3$ condensates by PLA of oxygen-purged Al target [33]. The defect clusters in the present case of γ-Al_2O_3 are apparently affected by Ni dopant based on the following defect chemistry considerations.

The spinel-type γ-Al_2O_3 having Ni^{2+} dopant in the interstitial site ($Ni_i^{\cdot}$) would be volume/charge compensated by the aluminum vacancies ($V_{Al}^{'''}$) and H^+ ($h^{\cdot}$) in association with noncharged oxygen atom (O_O^x) to form defect clusters [$Ni_i^{\cdot\cdot} + V_{Al}^{'''} + h^{\cdot} + O_O^x$], where the state of the individual point defect in the parenthesis is as defined, through the following equation in Kröger–Vink notation [34]:

$$NiO \xrightarrow{Al_2O_3} \left[Ni_i^{\cdot\cdot} + V_{Al}^{'''} + h^{\cdot} + O_O^x\right] \quad (1)$$

Alternatively, Ni^{2+} (0.055 and 0.069 nm) could substitute for smaller-sized Al^{3+} (0.039 and 0.054 nm) with specified ionic radii [35] in coordination number 4 and 6, respectively, in parenthesis, to form Ni'_{Al} coupled with the generation of volume compensating $V_{A1}^{'''}$ and charge compensating $h^{\cdot}$ to form defect clusters by the following equation:

$$NiO \xrightarrow{Al_2O_3} [Ni'_{Al} + V_{Al}^{'''} + 4h^{\cdot} + O_o^x] \quad (2)$$

The Ni-doped γ-Al_2O_3 condensate then has above defect clusters (i.e., by Eqn. 1 or 2) distributed in a paracrystalline manner within the spinel lattice. The observed interspacing of the defect clusters in the Ni-doped γ-Al_2O_3 condensates is ca. 1 nm (Fig. 5), which is close to that observed in γ-$Al_{2-\delta}O_3$ produced by PLA of oxygen-purged Al target [33] but significantly smaller than that (ca. 3 times difference) in statically fired $Co_{3-\delta}O_4$ [31] and Zr-doped $Co_{3-\delta}O_4$ [32] with the spinel isostructure.

As for the Ni-doped γ-Al_2O_3 nanocondensates, it showed intimate intergrowth of θ-Al_2O_3 (JCPDS file 11-0517) and commensurate superstructures, which have little to do with Ni dopant (presumably <1 mol % according to the phase diagram [28]) as such coarsening-induced intergrowth and shuffling were also observed for the H^+ and Al^{2+} doped γ-Al_2O_3 condensates formed by PLA of Al plate in water [36].

4.3 Internal stress of $NiAl_2O_4$ powders subjected to laser pulses in water

Regarding the stress state of the predominant spinel-type phase in the form of either nanocondensates and/or micron-sized particles, its refined lattice parameters from the sample subjected to PLA under 10-mm water/focus height for 5 and 20 min (Table 3) are 0.8016 and 0.8007 ± 0.0001 nm, respectively, which are significantly smaller than the

Table 3 Observed and refined XRD d-spacings (±0.0001 nm) for $NiAl_2O_4$ powders subjected to laser pulses for 0, 5 and 20 min in DI water to have the refined lattice parameter $a = 0.8046$, 0.8016 and 0.8007 nm, respectively

hkl	Observed			Refined		
	0 min	5 min	20 min	0 min	5 min	20 min
111	0.4643	0.4607	0.4595	0.4645	0.4631	0.4628
220	0.2847	0.2833	0.2829	0.2844	0.2834	0.2831
311	0.2424	0.2415	0.2412	0.2426	0.2417	0.2414
400	0.2013	0.2004	0.2002	0.2011	0.2004	0.2002
422	0.1644	0.1544	0.1544	0.1642	0.1543	0.1541
511	0.1549	0.1419	0.1418	0.1548	0.1417	0.1415
440	0.1423	NA	NA	0.1422	NA	NA
533	0.1227	NA	NA	0.1227	NA	NA
444	0.1162	NA	NA	0.1161	NA	NA
731	0.1048	NA	NA	0.1047	NA	NA

ambient value of starting $NiAl_2O_4$ powders (0.8046 nm, JCPDS#10-0339). This indicates a significant internal compressive stress, up to 5.9 GPa based on Birch–Murnaghan equation and bulk modulus $B_o = 372$ GPa along with its pressure derivative $B_o^{'} = 2.93$ GPa as determined for stoichiometric $NiAl_2O_4$ powders by static compression experiments [37]. Such a high stress level is apparently overestimated as Al enrichment also causes a smaller cell volume for nonstoichiometric $NiAl_{2+x}O_4$ spinel [38].

The inversion parameter that measures the extent of Al occupation in tetrahedral sites of nickel aluminate spinel, increases with the increase of applied pressure up to 35 GPa [37]. Al enrichment was also known to cause nickel vacancies and ordering to form spinel superstructure of nickel aluminate [39–42]. The combined effects of internal compressive stress and Al enrichment for the spinel condensate/particle not only caused a smaller cell volume, but also significant change of structure units as manifested by the modified Raman E_g/T_{2g} (both are O_h, i.e., m3m point group) and A_{1g} (D_{4h}, i.e., 4/mmm point group) vibration modes (Table 1).

4.4 Implications of optical property and phase changes of $NiAl_2O_4$ by PLA in water

The colloidal aqueous suspension containing the protonated $NiAl_{2+x}O_4$ fragments and newly condensed nanoparticles of 1-D lamellae, β-$Ni(OH)_2$, Al-doped NiO and Ni-doped γ-Al_2O_3 by the present PLA process showed a narrower minimum band gap (5.3 eV) than the starting $NiAl_2O_4$ powder (5.8 eV) [23]. The band gap lowering can be attributed to the combined effects of internal compressive stress, protonation/hydroxylation and phase change of $NiAl_2O_4$ powders. The resultant protonated composite nanoparticles of the NiO–Al_2O_3 composition system by the clean PLA synthesis in water have beneficial high-specific surface area and modified band gap for potential applications as catalytic support in view of the applications of $NiAl_2O_4$ [3, 4], NiO [5] and Al_2O_3 [6] as catalytic supports.

5 Conclusions

1. $NiAl_2O_4$ powders subjected to Q-switched laser pulses in water were fragmented as micron-sized $NiAl_{2+x}O_4$ spinel particles and decomposed as atom clusters for condensation nucleation as Al-doped NiO and Ni-doped γ-Al_2O_3 nanoparticles in a matrix of precursor hydroxides, i.e., 1D lamellae and β-$Ni(OH)_2$.
2. The $NiAl_{2+x}O_4$ fragments showed dislocations, subgrain boundaries and Al enrichment.
3. The Al-doped NiO and paracrystalline Ni-doped γ-Al_2O_3 nanoparticles tended to assemble as spherical polycrystals for surface area minimization.
4. The colloidal suspension containing the predominant protonated spinel phases, i.e., $NiAl_{2+x}O_4$ and Ni-doped γ-Al_2O_3, showed a lower minimum band gap for potential sensor applications, in particular as catalytic support of nickel like the case of stoichiometric $NiAl_2O_4$.

Acknowledgments We thank anonymous referee for constructive comments. This research was supported by Center for Nanoscience and Nanotechnology at NSYSU and partly by National Science Council, Taiwan, ROC.

Appendix

See Appendix Figs. 11 and 12.

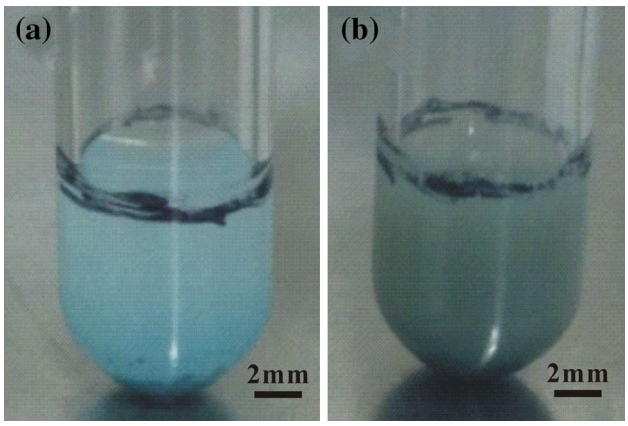

Fig. 11 Photos of colloidal suspension with immersed $NiAl_2O_4$ powders (*a*) before, (*b*) after PLA under 532 nm–400 mJ–10 mm–20 min conditions in DI water

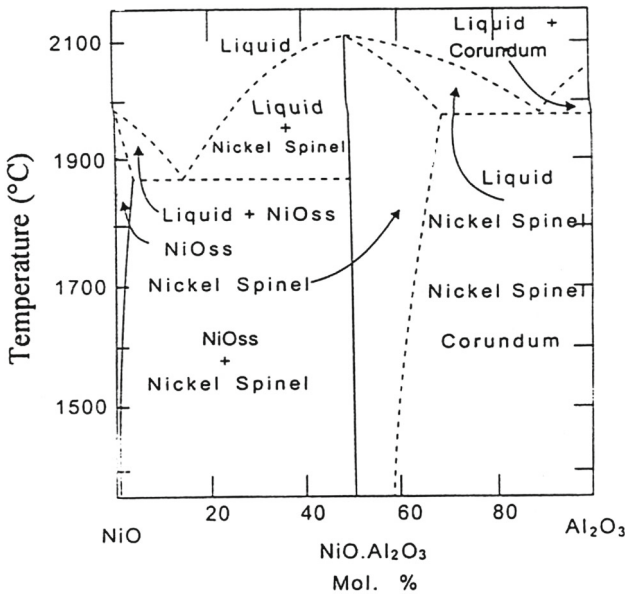

Fig. 12 $NiO–Al_2O_3$ phase diagram after Phillips et al. [28]. Note the nickel aluminate spinel ($NiAl_{2+x}O_4$) varies in composition from 50 to ~62 and ~65 mol % Al_2O_3, rather than ~38 and ~35 mol % Al_2O_3 as addressed in the abstract and result section of Phillips et al. [28]

References

1. I. Halevy, D. Dragoi, E. Üstündag, A.F. Yue, E.H. Arredondo, J. Hu, M.S. Somayazulu, J. Phys. Condens. Matter **14**, 10511 (2002)
2. L. Kou, J.R. Selman, J. Appl. Electrochem. **30**, 1433 (2000)
3. A. Al-Ubaid, E.E. Wolf, Appl. Catal. **40**, 73 (1988)
4. Y.P. Cesteros, F. Salagrem, M. Medina, J.E. Sueiras, Chem. Mater. **12**, 331 (2000)
5. A. Villa, G.M. Veith, D. Ferri, A. Weidenkaff, K.A. Perry, S. Campisi, L. Prati, Catal. Sci. Technol. **3**, 394 (2013)
6. G.V. Sagar, P.V. Rao, C.S. Srikanth, K.V. Chary, J. Phys. Chem. B **110**, 13881 (2006)
7. S.R. Wang, P. Shen, J. Solid State Chem. **140**, 38 (1998)
8. S.R. Wang, P. Shen, Mater. Sci. Eng. A **251**, 106 (1998)
9. C.O. Arean, M.P. Mentrait, A.J.L. Lopez, J.B. Parra, Colloids Surf. A Physicochem. Eng. Aspects **180**, 253 (2001)
10. H. Cui, M. Zayat, D. Levy, J. Non-Cryst, Solids **351**, 210 (2005)
11. M.M. Amini, L. Torkian, Mater. Lett. **57**, 639 (2002)
12. P. Jeevanandam, Y. Koltypin, A. Gedanken, Mater. Sci. Eng. B **90**, 125 (2002)
13. H.D. Lu, B.C. Lin, S.Y. Chen, P. Shen, J. Phys. Chem. C **115**, 24577 (2011)
14. P.W. Lin, C.H. Wu, Y. Zheng, S.Y. Chen, P. Shen, J. Phys. Chem. Solids **74**, 1281 (2013)
15. K.A. Carrado, A. Kostapapas, S.L. Suib, Solid State Ion. **26**, 77 (1998)
16. V. Rives, S. Kannan, J. Mater. Chem. **10**, 489 (2000)
17. S. Velu, K. Suzuki, M.P. Kapoor, S. Tomura, F. Ohashi, T. Osaki, Chem. Mater. **12**, 719 (2000)
18. Z.P. Xu, H.C. Zeng, J. Phys. Chem. B **104**, 10206 (2000)
19. F. Cavani, F. Trifiro, A. Vaccari, Catal. Today **11**, 173 (1991)
20. E.D. Rodeghiero, J. Chisaki, E.P. Giannelis, Chem. Mater. **9**, 478 (1997)
21. W.D. Nesse, *Introduction to optical mineralogy*, 2nd edn. (Oxford University Press, Oxford, 1991)
22. M.A. Laguna-Bercero, M.L. Sanju′an, R.L. Merino, J. Phys. Condens. Matter **19**, 186217 (2007)
23. Y.T. Chan, MS Thesis, National Sun Yat-sen University, Taiwan, 2013
24. H.D. Jang, S.K. Friedlander, Aerosol Sci. Technol. **29**, 81 (1998)
25. A. Navrotsky, C. Ma, K. Lilova, N. Birkner, Science **330**, 199 (2010)
26. A. Navrotsky, Geochem. Trans. **4**, 34 (2003)
27. I.L. Liu, P. Shen, S.Y. Chen, J. Nanopart. Res. **12**, 2929 (2010)
28. B. Phillips, J.J. Hutta, I. Warshaw, J. Am. Ceram. Soc. **46**, 579 (1963)
29. C.N. Huang, S.Y. Chen, P. Shen, J. Phys. Chem. C **111**, 3322 (2007)
30. C.H. Chen, C.N. Huang, S.Y. Chen, P. Shen, J. Nanopart. Res. **13**, 3683 (2011)
31. W.H. Lee, P. Shen, J. Solid State Chem. **177**, 101 (2004)
32. M.Y. Li, P. Shen, Mater. Sci. Eng. B **111**, 82 (2004)
33. J.N. Pan, PhD Thesis, National Sun Yat-sen University, Taiwan, 2006
34. F.A. Kröge, H.J. Vink, Solid State Phys. **3**, 307 (1956)
35. R.D. Shannon, Acta Crystallographica A **32**, 751 (1976)
36. I.L. Liu, P. Shen, S.Y. Chen, J. Phys. Chem. C **114**, 7751 (2010)
37. L. Halevy, D. Dragoi, E. Üstündag, A.F. Yue, J. Phys. Condens. Matter **14**, 10511 (2002)
38. D. Keiji, I. Toshihiro, H. Yasuo, O. Toshitaka, J. Chem. Soc. Jpn. Chem. Ind. Chem. **2**, 195 (2002)
39. E. Üstündag, R. Subramanian, R. Dieckmann, S.L. Sass, Acta Metall. Mater. **43**, 383 (1995)
40. J. Noack, D.X. Hammer, G.D. Noojin, A. Vogel, J. Appl. Phys. **83**, 7488 (1998)
41. J. Noack, A. Vogel, IEEE J. Quantum Electron. **35**, 1156 (1999)
42. A. Vogel, V. Venugopalan, Chem. Rev. **103**, 577 (2003)